**Authors Version**

# Study of CMAS infiltration and evaporation behaviour under water vapour/sulphur oxide conditions in EB-PVD 7YSZ

X. Montero [a,*], R. Naraparaju [b], M.C. Galetz [a] and U. Schulz[b]

[a] DECHEMA-Forschungsinstitut, High Temperature Corrosion Team, Theodor-Heuss-Allee 25, 60486, Frankfurt, Germany

[b] DLR (German Aerospace Center), Institute of Materials Research, Cologne, Germany

**Corrosion Science 198 (2022) 110123**

**https://doi.org/10.1016/j.corsci.2022.110123**

# Study of CMAS infiltration and evaporation behaviour under water vapour/sulphur oxide conditions in EB-PVD 7YSZ

X. Montero [a,*], R. Naraparaju [b], M.C. Galetz [a] and U. Schulz[b]

[a] DECHEMA-Forschungsinstitut, High Temperature Corrosion Team, Theodor-Heuss-Allee 25, 60486, Frankfurt, Germany

[b] DLR (German Aerospace Center), Institute of Materials Research, Cologne, Germany

## ABSTRACT

The infiltration behaviour of $CaO$-$MgO$-$Al_2O_3$-$SiO_2$ (CMAS) in Electron Beam Physical Vapour Deposited (EB-PVD) 7 wt.% yttria stabilized zirconia (7YSZ) under controlled atmospheres (dry, wet and sulphurizing) was studied in detail. The microstructure of the

CMAS-infiltrated 7YSZ and the CMAS residue on top were analysed to interpret the corrosion mechanisms. One of the major goals was to investigate the stability and the infiltration of $CaSO_4$ into the 7YSZ columns. At the testing temperature of 1250°C, $CaSO_4$ was stabilized only under the $SO_2$ atmosphere within the TBC coating and only in $CaSO_4$-containing CMAS. Hydroxylation of CMAS elements was found under wet conditions, which changed the local CMAS composition and infiltration behaviour. These chemistry changes have provoked acidity changes in the CMAS which directly affected their aggressivity and viscosity. Thermodynamic equilibrium predictions on the volatility of CMAS components and the anhydrite stability under various atmospheres were used to understand the experimental findings and the underlying mechanisms.

## 1. INTRODUCTION

It is commonly accepted that the major form of Thermal Barrier Coating (TBC) degradation by CMAS is liquid-phase infiltration into the TBC that causes a reduction in strain compliance (stiffening) of the coating and an increase in thermal stresses during cooling [1-4]. This mechanism is particularly relevant to EB-PVD TBCs, which have a network of open channels in the form of inter-columnar gaps spanning through the whole thickness of the coating. CMAS infiltration is driven by capillarity, and its penetration depth depends on temperature, time, chemical composition, and viscosity of the CMAS melt [5,6]. Chemical attack of 7YSZ by CMAS is another classical corrosion issue that occurs in the form of yttria dissolution and diffusion out of the TBC into the molten CMAS [1, 7-9]. It is followed by mechanical degradation when eventually tetragonal to monoclinic phase transformation of the 7YSZ accompanied by cracking takes place [10-12]. On ex-service parts deposits containing anhydrite were often found [2,10,13,14]. The source of anhydrite in the TBCs in aviation

engines is ingested gypsum dust originating from sediments near runways or industrial emissions as well as $SO_2$ present in jet fuel which might react with the CaO of CMAS to form anhydrite. In engine atmospheres, the $SO_2$ partial pressure is not only controlled by the combustion of jet fuel (maximum S content is 0.3 wt%, but typically below 0.1 wt%) but also by compressed air. In stationary gas or marine turbines, Ca and S levels of the fuel are generally higher, causing the formation of higher $CaSO_4$ contents. Sulphur and sodium were also found on dove-tail regions of high-pressure turbine blades of ship gas turbines, and it is believed that the source might be the mix of fuel and sea salt which causes a unique kind of corrosion damage [15]. Infiltration and deposition of $CaSO_4$ within TBCs in combination with/out CMAS deposits have been found on many occasions on real aviation engines and stationary turbines [16-21]. However, the effect of $CaSO_4$ on CMAS-induced TBC damage is not clear yet, and related research is rare. Even the main location of degradation related to anhydrite-holding CMAS deposits in real turbines is not clear. $CaSO_4$ was observed on top of the TBC in few studies and within the colder zone of the TBC columns in another study [2]. Although Ca is also present in the hotter outer zone, it has not been sulphatized in the described case, which shows the operating conditions in the engine would allow both CaO and anhydrite infiltration simultaneously. Additionally, both areas are separated by a distinct Ca-free gap of several tenths of microns which could not be understood so far. This scenario suggests a possible vapour phase transport of $Ca(OH)_2$ as reported in the literature [22]. This phenomenon could not be observed in any laboratory study (all studies we are aware of were carried out in lab air). In one of our previous studies, a realistic CMAS composition with $CaSO_4$ (relying on the real engine deposit data) was synthesized, and its influence on the CMAS infiltration behaviour in an EB-PVD 7YSZ coating was investigated at 1225-1250°C in isothermal conditions in air without a temperature gradient [23]. This study revealed that $CaSO_4$-containing CMAS was more aggressive with respect to 7YSZ dissolution and the infiltration depth was higher than

with its pure CMAS counterpart. However, after the experiments, $CaSO_4$ was not found in the CMAS, i.e. $CaSO_4$ was dissociated during the infiltration experiments in contradiction to findings on engine hardware. The dissociation of $CaSO_4$ into CaO and $SO_3$ was confirmed at 1050°C in laboratory air under the presence of CMAS using mass spectroscopy and in-situ high-temperature XRD [23,24]. $CaSO_4$ decomposition in the presence of CMAS is related to the formation of low-melting eutectic mixtures. Therefore it is believed that, if enough $SO_2$ is present in the atmosphere along with water vapour, a gaseous phase transport of $CaSO_4$ into the TBC could be possible. The importance of condensation of species in CMAS degradation has been investigated by Tolpygo et al. [22, 25]. The proposed mechanism reveals the importance of hydroxylation and vapour transport of the constituent CMAS oxides and hydroxides, respectively. Future concepts such as hydrogen combustion or wet aero-engines would cause approximately 3-4 times higher water vapour contents in the combustion chamber. Hence, it is worthwhile to investigate the CMAS infiltration study under water vapour and along with sulphur-oxide in the atmosphere. In order to understand the effect of volatility and sulphidation of CMAS on the infiltration behaviour and the stability of $CaSO_4$, high-temperature infiltration tests under dry/wet synthetic air along with and without sulphur atmospheres were conducted. The experimental results are discussed in the shed of the volatility behaviour of individual constituents of CMAS as predicted by using thermodynamic calculations.

## 2. EXPERIMENTAL PROCEDURE

The tested CMAS simulates compositions reflecting those of different aero-engine parts which were used in flights over middle-east countries [1, 16]. Based on analyses performed in previous works [10, 23], two CMAS variants were selected (see table 1). The difference

between CMAS1 and CMAS2 is the addition of 20% wt. of anhydrite ($CaSO_4$) in CMAS2. Both CMAS compositions were synthesized by co-decomposition of Me-nitrates (Me = Al, Ca, Mg, Fe) together with $SiO_2$ and $TiO_2$ powders according to the methodology described in [10]. The melting process of CMAS1 begins between 1200 °C and 1210 °C and ends between 1230 °C and 1250 °C. The onset and peak melting temperature of CMAS2 are approximately 15 K lower than that of CMAS1 [10].

Around 10 mg/cm$^2$ of these two CMAS variants were applied on 400 µm thick 7YSZ EB-PVD coatings deposited on an alumina substrate. The standard microstructure obtained was named as "Normal" and the corresponding process parameters were given elsewhere [26]. Isothermal infiltration experiments were conducted at 1250°C in a horizontal alumina tube for 5 hours. The infiltration tests were conducted under 1) dry synthetic air, 2) wet synthetic air with 10 vol.% $H_2O$, 3) dry synthetic air with 0.5 vol. % $SO_2$ and 4) wet synthetic air with 10 vol.% $H_2O$ and 0.5 vol. % $SO_2$.

The microstructure and composition of the cross-sections were characterized using field emission scanning electron microscopy (SEM) combined with energy-dispersive X-ray spectroscopy (EDX) (Hitachi SU5000). Electron probe microanalysis (EPMA; JEOL JXA-8100) with a spatial resolution close to 1 µm was used to quantify the concentrations of the different elements via element distribution maps, line scans, and point analysis using an excitation energy of 15 kV. Thermodynamic calculations were performed with FactSage version 6.1 to estimate the stability and quantity of the different CMAS species.

## 3. RESULTS

After high temperature exposure, all of the CMAS2-infiltrated samples have no CMAS residue on top of the YSZ, whereas on the CMAS1 samples some residue was still present on top of

the YSZ (see figure 1). Moreover, the wetting and spreading of CMAS2 on the surface are more prominent than that observed with CMAS1.

Figure 2 shows the cross-sections of the CMAS1- and CMAS2-deposited YSZ after 5h of heat treatment under synthetic air with 0.5 vol. % $SO_2$. Other samples will not be shown to avoid the reiteration of figures. Based on the SEM cross-sectional analysis, it was found that YSZ coating was completely infiltrated under all the environmental conditions that were used. According to the experimental conditions, both tested CMAS compositions were fully molten during the exposure. The absence of CMAS2 residue on top of the YSZ demonstrates that the melting temperature of CMAS is not the unique reason for infiltration, and that the composition-dependent surface wettability of the CMAS itself plays a vital role in the infiltration mechanism, as will be shown in the following.

## 3.1. CMAS1 infiltration behaviour

### *3.1.1. Observations of CMAS residue on top of infiltrated YSZ*

The cross-section of the CMAS1 residue on top of infiltrated YSZ coating (5h exposure at 1250°C) under dry conditions is shown in figure 3. A high magnification image of the CMAS residue without $SO_2$ is shown in figure 3a. The CMAS residue shows two main phases (a bright and a dark) and a minor bright-coloured dispersed phase only present very locally. The bright phase presents low Si and high Mg, Ti and Fe compared to the dark phase. It is mainly localized at the CMAS1/gas interface, and its composition matches with pyroxene. The dark phase shows a composition rich in Si and Al with much lower Mg, Ti and Fe contents. It is an anorthite phase and is mainly localized at the CMAS1/YSZ interface. The composition of the white spots has not been analysed in this case due to the small spot size, but the elemental distribution map (not shown) reveals that they are mainly composed of Fe and Mg in oxide

form. Additionally, the solubility of Y and to a minor amount Zr in the pyroxene can be confirmed in the pyroxene.

The CMAS residue of dry synthetic air with 0.5 vol.% $SO_2$ exposure exhibits the same two main phases (compare figure 3a and 3b) and two small white coloured. The composition of the anorthite and pyroxene is quite similar in both dry atmospheres (see table 2). The two small bright precipitates can also be identified in figure 3b. The fine, randomly distributed ones are Y- and Zr-rich and the larger ones are Fe-, Mg- and Al-rich (see figure 3c). Compared to the exposure in dry synthetic air, the main difference is the higher presence of Y and Zr precipitates located either close to or encircled by the anorthite phase in the case of $SO_2$-containing atmosphere.

Figure 4 shows the CMAS1 residue after exposure under wet conditions. The main difference compared to the dry atmosphere exposure cases is that the anorthite phase exhibits around 10 wt.% Si (compare tables 2 and 3). The analysis of the sample exposed to water vapour and $SO_2$ confirms the previous observation. The formation and evaporation of hydroxide species as $Si(OH)_4$ under water vapour-containing atmosphere is believed to be the main reason for this difference. It is interesting to note that the composition of anorthite and pyroxene phases does not show any gradient. On the contrary, it was uniform in the whole remaining CMAS1 independent of the location of the analysis. i.e. the evaporation of hydroxides under the applied conditions occurs fast, and no gradual effect can be observed in the depth of the CMAS1 deposit. In any of the exposure conditions was confirmed the presence of S in the CMAS1

#### *3.1.2. YSZ-CMAS interface*

The extent of Y and Zr dissolution with respect to the infiltrating conditions has been pointed in the previous section but becomes more obvious with the analysis of the YSZ at the CMAS interface.

The YSZ was analysed by EPMA for all exposure conditions. The results seem very similar for all of the studied cases. Therefore, only wet synthetic air is shown in figure 5 to avoid reiteration. EPMA analysis reveals depletion of Y in the uppermost columns of YSZ. This depletion in Y is directly reflected by Y enrichment in the anorthite phase and by the formation of pores in the YSZ grains at the coating/residue interface (see figure 6). Al enrichment directly at the CMAS1/YSZ interface (shown in figure 5) proves the fact that the anorthite phase is more concentrated at the coating/residue interface, and the enrichment of Ti, Fe at the residue/gas interface suggests that the pyroxene acts as a sink for all of the other elements. Mg depletion is also observed in the CMAS residue close to the YSZ interface. The occurrence of such depletion is more evident under water vapour atmospheres (figures not shown), which might serve as a proof for possible Mg evaporation that is discussed later.

The amount of dissolved Y at the CMAS1/YSZ interface seems to be influenced by the exposure atmosphere. In the case of $SO_2$ free atmospheres, the Y depleted YSZ has a thickness of 10µm of and is mainly localized at the YSZ column rims (see figure 6a). This effect is reinforced with the addition of $SO_2$. Figure 6b shows extended intra-columnar porosity in YSZ where not only the periphery (column tips and feathery porosity) but also the core of the YSZ is affected by the Y depletion.

#### *3.1.3. YSZ-$Al_2O_3$ interface*

The changes observed due to the presence of CMAS on the $Al_2O_3$ substrate can serve to interpret the possible modifications occurring on the thermally grown oxide scale formed on top of a bond coat.

The detailed analysis of the YSZ/alumina interface is shown in figure 7 using EDX elemental mapping. In all cases the inter-columnar gaps of YSZ were replenished by Ca and Si. The reaction product formed between the YSZ and the $Al_2O_3$ is comprised of two distinct layers. The one closer to the YSZ is an oxide rich in Ca, Si and Al (probably anorthite), whereas the one close to the $Al_2O_3$ is an oxide consisting of Mg and Al (probably spinel). This Mg- and Al-based oxide is continuous in the cases of dry and wet synthetic air but shows a non-homogeneous layer thickness in the cases in which $SO_2$ is present in the gas. The overall thickness of this reaction layer seems to be larger under wet atmospheres compared to dry conditions.

## 3.2. CMAS2 infiltration behaviour

### *3.2.1. CMAS-YSZ interface*

As described previously, the CMAS2 samples showed no glass residue on top of the YSZ after infiltration. Figure 8a shows the BS-SEM cross-section and the EPMA elemental distribution map of one sample after exposure in dry synthetic air as an example to show that full infiltration took place. Surprisingly, S was found only in the middle section of the YSZ coating. Nevertheless, a detailed analysis shown in figure 8b reveals that S is mainly located in pores in combination with Cl and C from the mounting epoxy resin and not with oxygen, CMAS, or YSZ elements. Therefore, to avoid misinterpretation, extreme care has been procured with the S analysis of the samples.

The only cases of CMAS2 in which S is bonded to Ca as $CaSO_4$ is the ones containing $SO_2$ in the gas. Figure 9 shows the case of the wet atmosphere with 0.5vol.% $SO_2$ as a mode of example. The $CaSO_4$ is located at the outermost EB-PVD coating area. This indicates that the required parameters to form or maintain $CaSO_4$ match only at the boundary conditions obtained in this position.

Figure 10 compares the EPMA-measured composition of the infiltrated CMAS1 and CMAS2 in the YSZ. The analysis was performed in areas with significant CMAS quantities to avoid signals from the surrounding YSZ. The composition of the infiltrated CMAS1 (figure 10a) did not reveal any important differences depending on the exposure atmosphere. No S was detected in the infiltrated CMAS1 melt. Therefore, it can be clearly concluded that the $SO_2$ of the tested atmosphere was not sufficient to react to sulphates with CMAS1. Contrarily, S was detected in the case of CMAS2. In exposure without $SO_2$, the identified S was below the quantification limit. With atmospheres containing 0.5% $SO_2$ (dry and wet), most of the S is located in the upper part of the YSZ, as shown in figure 9. The identified S amount is higher in the case of the wet sulphurising (10 vol.% $H_2O$ + 0.5 vol.% $SO_2$) atmosphere than in the case of the dry one. Therefore, the role of water vapour in the stabilization of $CaSO_4$ will be further investigated. The quantitative differences between CMAS1 and CMAS2 in the rest of the analysed elements (Si, Fe, Ti, Mg, Ca and Al) directly reflect the compositional differences (compare CMAS1 and CMAS2 of table 1).

### *3.2.2. YSZ-$Al_2O_3$ interface*

Similar to CMAS1, Mg- and Al-containing spinel has formed at the YSZ/alumina interface. The most relevant difference is that in the case of CMAS2 a continuous spinel formation

occurred in $SO_2$-containing atmospheres (see figure 11) while the $SO_2$-free conditions produced similar interface layers as shown in figure 7.

The statistical analysis of the anorthite + spinel layer thickness formed at the interface in the YSZ and alumina is shown in figure 12 for all cases of both CMAS1 and CMAS2. As the spinel thickness is quite irregular among the studied cases, cumulative plots were drawn to obtain an accurate estimation of the thickness. The cumulative probability represents the amount of the analysed area showing a given value of spinel thickness. e.g., the thicknesses given at 0.8 of the cumulative probability % indicate the minimal spinel thickness for 80% of the analysed area. So, for CMAS1 in the dry atmosphere without $SO_2$, 80% of the measured spinel has at least 4 µm thickness, whereas, for the wet atmosphere without $SO_2$, the same analysed area gives a minimum thickness of 7 µm. In both CMAS cases the lowest mean thickness (probability 0.5) is obtained for dry synthetic air followed by dry synthetic air with $SO_2$. Thus, thicker layers are present in the case of wet gases. A notable difference between the highest and the lowest thickness value through the probability plot is usually a clear indicative of irregular spinel layers. This effect can be observed in the CMAS1 (figure 12a) case in which the wet atmosphere exposure shows a steeper gradient than the dry ones. This irregularity in spinel thickness is less pronounced for CMAS2 than for CMAS1. Overall, the figure indicates that the corrosion product is thicker in wet atmosphere and CMAS2 produces a more regular thickness spinel than CMAS1.

## 4. DISCUSSION

Based on the isothermal infiltration experiments performed at 1250°C under different atmospheres, the significant differences between the infiltration behaviour of the two used CMAS compositions in EB-PVD YSZ are summarized in the following table 3. The current

results clearly indicate the importance of studying the interplay between water vapour, $SO_2$ in the atmosphere, and the CMAS corrosion behaviour since both lead to substantial changes in infiltration kinetics, phase formation or reactions with an alumina layer. The most important parameters for the explanation of the observed phenomena will be explained in the discussion.

It is known from literature that 7YSZ offers no resistance to CMAS infiltration, which can lead to thermomechanical failure of the coating [7,8,10]. The reactivity of 7YSZ with CMAS is too slow to cause a crystalline reaction product at the interface, thus not stopping the CMAS infiltration [1,9]. This fact has once again been proven even under the presence of water vapour in this study. It has been shown that the viscosity of CMAS2 is lower than the one of CMAS1, which has a significant impact on the infiltration behaviour [6,23,26]. This effect can be seen in figure 1 and figure 2, in which no CMAS residue was left on the coating after exposure at 1250°C for CMAS2. At the same time, more surface area of the substrate was covered with CMAS2 melt. This can be due to a lower contact angle, which spreads over the surface and wets it [6]. In both cases, the infiltrated CMAS glass reaches the TBC/alumina interface and reacts with the alumina to form a spinel layer. The reaction layer thickness (anorthite + spinel) at the interface in the case of CMAS2 is thicker and more homogeneous than that of CMAS1, which conveys that more residue is present at the alumina interface with CMAS2. In one of the previous studies, $CaSO_4$ within the CMAS was found to be dissociated above 1100°C under lab air conditions, which has caused a decrease in the viscosity of the melt [23]. However, due to the different atmospheres used in the study, parallel sulphatization and evaporation of individual oxides of CMAS may have started, which in turn changed the overall solubility of YSZ in the melt. This can be explained based on the following discussion.

### 4.1. Solubility of YSZ in CMAS and acidity of the melt

The solubility of Y and Zr oxides in the CMAS has been explained by Levi et all [1] in dry air. The solubility of oxides in complex atmospheres can be explained by applying the well-known principles of Rapp et al. [27,28], which describe the solubility principle of the hot corrosion mechanism in type I conditions. Type I hot corrosion is observed when a molten deposit, typically sodium sulphate, reacts with the oxide scales and provokes their dissolution from the scale and reprecipitation in the melt. This solubility provokes a depletion profile in the corroded substrate simultaneously. The solubility of oxides in molten salts depends on the acidity/basicity of the melt following the Lux-Flood concept of acid/base reactions [29], where acid is the oxide-ion acceptor (e.g. $Na^{+}$, $Si^{4+}$) while a base is an oxide-ion donor (e.g. $Na_2O$, $Y_2O_3$, $ZrO_2$). In this concept, the local activity of $O^{2-}$ in the molten salt determines which of the acid/base is thermodynamically stable. Therefore it is expected that basic oxides as $Y_2O_3$ and at lower level $ZrO_2$ react with acidic ones such as the silica in the melt. According to Rapp, the reprecipitation of the dissolved oxides at the gas/CMAS1 interface is also an evidence of the solubility principle [27,28]. For example, this effect can be seen in figure 3, where $Y_2O_3$ precipitates were present in the CMAS1 melt. In cases in which the negative solubility gradient is maintained, the dissolved oxides precipitate in the outer interface of the deposit (atmosphere side) and can be found at higher quantities in pyroxene. Similar dissolution and reprecipitation reactions were also observed for the dissolution of YSZ in vanadate deposits by Jones et al. [30]. Also the optical basicity [31] has been used by several research groups to explain the reaction between CMAS and coatings, therefore they classify the deposit behaviour based on relative Lewis acid-base reactions. Vilasi and co-workers tried to understand and predict the dissolution of coating materials into a CMAS [32, 33] and Krause and co-workers worked on selecting the most adequate coating materials with a tailored protective reaction [34, 35]. The results presented indicate that the acidity/basicity of the melt not only depends on the CMAS

composition but also in the exposure atmosphere composition. Additions of $SO_2$ increase the acidity of the melt and increases the solubility of Y or Zr.

The acidity of the CMAS is vital for the solubility mechanism but also for the physical properties of the melt. The basicity index is often related to the viscosity of the melts [36]. Acidic oxides tend to enhance the polymerization of the melt and consequently have higher viscosities, whereas basic oxides tend to disrupt the polymerization process. Consequently, basic melts present lower viscosities [37]. Any compositional change in the melt, but especially those in the very acidic or highly basic compounds of the melt, will consequently affect its viscosity and infiltration velocity in the YSZ. Therefore, the stability of the CMAS compounds at the different exposure conditions will be discussed below.

In order to understand the effect of water vapour on the CMAS infiltration behaviour and on the stability of sulphates within the TBCs, thermodynamic equilibrium simulations were performed, and the results are correlated with the experimental findings.

### 4.2. Stability of sulphates

Due to the presence of $SO_2$ in the exposure gases, the formation of new sulphates along with $CaSO_4$ during the high-temperature exposure is expected in both CMAS melts. At the same time, the stability of the $CaSO_4$ in CMAS2 should also be evaluated under $SO_2$-free atmosphere. In any case, sulphate formation may provoke an increase in the melt acidity, whereas the $CaSO_4$ dissociation may increase the basicity of the melt.

The calculations of the most relevant sulphates as a function of temperature and $SO_3$ partial pressure by FactSage are shown in figure 13 (aluminium, iron and titanium sulphates are not

stable at the selected temperature range). The activity of the metal oxides is unity for pure oxides but is usually reduced in CMAS mixtures. This effect was not corrected in the calculations, which means that the presented calculated partial pressures are slightly higher than in reality. It also has to be noted that the calculations neglect the effect of different elements solution in the CMAS, e.g. Y and Zr. This figure also shows different $SO_2$ concentration lines for a more informative lecture of the diagram. No significant differences were found between dry and wet synthetic air in such calculations; therefore, the figure only represents the results of wet synthetic air. It can be seen that the stability of $MgSO_4$ is lower than that of $CaSO_4$ and that above 1100°C $MgSO_4$ is not stable anymore. At 1250°C, more than 0.1 % $SO_2$ is required to stabilize $CaSO_4$, and (as confirmed in the experiments) the tested $SO_2$ value of 0.5% should be enough to find stable $CaSO_4$ or to form $CaSO_4$ from CaO within in CMAS. The diagram also reveals that, if $MgSO_4$ is present in the CMAS initially, its dissociation at high temperature (above 1100°C) would release $SO_3$ and increase its partial pressure, consequently increasing the possibilities of stabilizing the $CaSO_4$. Thus it is reasonable to say that at the used experimental conditions $CaSO_4$ is the only stable sulphate among all the other possible sulphates. However, the situation might change under volatile hydroxides formation, which will be discussed later.

The calculated quantification of the formed $CaSO_4$ for 1 mol of the tested CMAS compositions during the different exposure conditions is shown in figure 14. For CMAS1, $CaSO_4$ is only present in $SO_2$-containing atmospheres and only up to 1100°C. At temperatures above 1100°C, $CaSO_4$ dissociates from CMAS1 and forms different liquid silicates. $CaSO_4$ is stable in CMAS2 under $SO_2$-free atmospheres up to 1200°C, and requires $SO_2$ presence to make it stable above 1200°C. The diagram shows that the exposure in dry $SO_2$ atmosphere presents more $CaSO_4$ than in the wet one, and the difference increases with increasing temperature. The

evaporation of Ca species in the wet atmosphere has a significant influence on this phenomenon. The presence of $CaSO_4$ in the cases of CMAS2 in wet and dry $SO_2$ shown in figure 9 validates this point. $CaSO_4$ was mainly observed at the outermost YSZ interface, this location presents the adequate $SO_2/SO_3$ activity. The typical gas species gradient through the YSZ layer reduces the amount of $SO_2$/ $SO_3$ and consequently the possibility of forming $CaSO_4$ in the middle of the YSZ. These calculations imply that anhydrite is more stable at a lower temperature. This implies that under realistic conditions, where a thermal gradient is also established in the TBC coating, the anhydrite stability zone increases. Therefore it can be found deep inside the YSZ and not only on top of the TBC. This could explain the presence of $CaSO_4$ at different locations of the TBC on real cases in turbine blades.

### 4.3. Evaporation of different species

The presence of water vapour as a combustion product in an aero-engine is a crucial element that dictates the condensation and evaporation species of CMAS. Most CMAS studies for YSZ have been done in dry atmospheres. The few cases of CMAS corrosion in wet atmospheres are related to environmental barrier coatings and no detail has been revealed about CMAS modifications due to the wet atmosphere [38, 39]. Thermodynamic simulations give a prognosis of evaporating species at the temperatures of interest and various gas mixtures. Figure 15 presents the calculations for CMAS1 and CMAS2 under wet synthetic air for a range of the temperatures of interest. Among all possible evaporating species, $SiO(OH)_2$ and $Si(OH)_4$ have a higher tendency to evaporate with $H_2O$. Other species showing high partial pressures are $Mg(OH)_2$ followed by $Ca(OH)_2$. Finally, a low partial pressure is also calculated for another Si species in $SiO_2$ which also evaporates as SiO(OH), but the value has been omitted in the diagram for easier visibility (also due to its proximity to the $Ca(OH)_2$ lines). The diagram reveals important differences between CMAS1 and CMAS2 between 1200-1300°C. Si species

seem to evaporate more from CMAS1, whereas Ca and Mg evaporate in the form of hydroxides from CMAS2 at temperatures above 1200°C. Such an elevated evaporation of Ca and Mg species from CMAS2 might be partially responsible for the thicker and homogeneous anorthite and spinel reaction layer formed at the YSZ/$Al_2O_3$ interface shown in figure 12. The evaporation of $Ca(OH)_2$ directly influences the amount of $CaSO_4$ formation, as shown in figure 14, where less anhydrite has formed under wet+$SO_2$ atmosphere in the case of CMAS2. The depletion of Mg at the CMAS/gas interface shown in figure 5 supports the assumption that Mg evaporation might happen under wet atmospheres. This kind of gaseous phase transport explains the spinel formation at the thermally grown bond coat scale of CMAS-corroded turbine blades, which has been experimentally demonstrated by Lutz et al. [22]. Similarly, Si evaporation directly influences aggressiveness of the melt by decreasing the viscosity of the residue.

Under water vapour, CMAS undergoes several changes in its chemistry and viscosity and it shows a peculiar volatility behaviour. The stability of anhydrite increases under wet conditions at high temperatures whose presence has an additional effect on the overall functionality of the TBCs. It is highly recommended to do such studies under wet atmospheres on CMAS-resistant TBCs such as GZO or 65YZ, where local changes in the CMAS chemistry influence the entire reaction mechanism. This study also directly implies CMAS/Environmental Barrier Coatings (EBC) interactions, and similar experiments must be performed under relevant gas compositions to understand the reaction mechanisms. This becomes even more important in the future, since, as mentioned in the introduction section, novel hydrogen combustion-based aero-engines would generate higher water vapour contents in the engine (up to 20-25%).

## 5. CONCLUSIONS

CMAS attack on EB-PVD 7YSZ under various atmospheres is studied in detail and corresponding effects on the dissolution and reprecipitation mechanism of the YSZ, on the volatility of individual oxides of CMAS on the stability/infiltration of $CaSO_4$ within the 7YSZ and the reaction of CMAS elements with the $Al_2O_3$ below the 7YSZ are explored. The dissolution of YSZ has been related to the acidity of the CMAS glass. Evaporation of different oxides of CMAS were observed under wet conditions. Modifications in CMAS composition due to the evaporation or sulphatization of different species affected the basicity and consequently the viscosity of the melt.

Apart from these general observations, the following conclusions can be made based on both the experimental results and thermodynamic equilibrium calculations.

1. Thermodynamics predicts that $CaSO_4$ is stable along with CMAS only up to 1100°C. At higher temperatures the stability of $CaSO_4$ drops drastically, and $SO_2$ is required to stabilize it.
2. The experiments under isothermal conditions revealed that $CaSO_4$ was only observed at the YSZ/gas interface after infiltration. The $SO_2$ activity gradient through the YSZ is believed to be the main reason.
3. The dissociation of $CaSO_4$ in CMAS2 under $SO_2$-free conditions provokes the release of $SO_3$ and the formation of $(CaMgSi)O_3$ liquid phase.
4. The presence of water vapour increases the evaporation of Mg and Ca species in CMAS2 and that of Si species in CMAS1. This implies a thicker spinel reaction layer at the TBC/alumina interface in CMAS2 and a reduction in the CMAS1 viscosity. As a result, the more basic melt is readily available at the TBC/CMAS interface, and more Y is dissolved in the melt in CMAS1, which leads to a higher Y depletion in the columnar rims.

**Acknowledgements**

The authors would like to thank Dr. G. Schmidt and M. Thalheimer from DECHEMA-Forschungsinstitut for performing EPMA and the SEM analysis. The authors also thank D. Peters and J. Brien for their assistance in producing the EB-PVD samples. Special thanks to A. Handwerk for his technical assistance in experimental testing.

**REFERENCES**

[1] Levi, C.G., Hutchinson, J.W., Vidal-Setif, M.H., Johnson, C.A., "Environmental degradation of thermal-barrier coatings by molten deposits", MRS Bulletin, 37(10) (2012) 932-941.

[2] Braue, W., Mechnich, P., Green,D.J., "Recession of an EB-PVDYSZ Coated Turbine Blade by $CaSO_4$ and Fe, Ti-Rich CMAS-Type Deposits", Journal of the American Ceramic Society, 94(12) (2011) 4483-4489.

[3] Schulz, U., Braue, W. "Degradation of $La_2Zr_2O_7$ and other novel EB-PVD thermal barrier coatings by CMAS ($CaO$-$MgO$-$Al_2O_3$-$SiO_2$) and volcanic ash deposits", Surface and Coatings Technology, 235 (2013) 165-173.

[4] Aygun, A., Vasiliev, A.L., Padture, N. Ma, X. "Novel thermal barrier coatings that are resistant to high-temperature attack by glassy deposits", Acta Materialia, 55(20) (2007) 6734-6745.

[5] Kabir, M.R., Sirigiri, A.K., Naraparaju, R., Schulz, U., "Flow Kinetics of Molten Silicates through Thermal Barrier Coating: A Numerical Study", Coatings, 9(5) (2019) 332.

[6] Naraparaju, R., Gomez Chavez, J.J., Niemeyer, P., Hess, K.U., Song, W., Dingwell, D.B., Lokachari, S., Ramana, C.V., Schulz, U., "Estimation of CMAS infiltration depth in EB-

PVD TBCs: A new constraint model supported with experimental approach", Journal of the European Ceramic Society, 39(9) (2019) 2936-2945.

[7] Darolia, R., "Thermal barrier coatings technology: critical review, progress update, remaining challenges and prospects", International Materials Reviews, 58(6) (2013) 315-348.

[8] Mercer, C., Faulhaber, S., Evans, A.G., Darolia, R., "A delamination mechanism for thermal barrier coatings subject to calcium–magnesium–alumino-silicate (CMAS) infiltration", Acta Materialia, 53(4) (2005) 1029-1039.

[9] Krämer, S., Yang, J., Levi, C.G., Johnson, C.A., "Thermochemical interaction of thermal barrier coatings with molten CaO-MgO-$Al_2O_3$-$SiO_2$ (CMAS) deposits", Journal of the American Ceramic Society, 89 (10) (2006) 3167-3175.

[10] Naraparaju, R., Schulz, U., Mechnich, P., Döbber, P., Seidel, F., "Degradation study of 7 wt.% yttria stabilised zirconia (7YSZ) thermal barrier coatings on aero-engine combustion chamber parts due to infiltration by different CaO–MgO–$Al_2O_3$–$SiO_2$ variants", Surface and Coatings Technology, 260 (2014) 73-81.

[11] Poerschke, D.L., Jackson, R.W., Levi, C.G., "Silicate Deposit Degradation of Engineered Coatings in Gas Turbines: Progress Toward Models and Materials Solutions", Annual Review of Materials Research, 47 (2017) 297-330.

[12] Jackson, R.W., Zaleski, E.M., Poerschke, D.L., Hazel, B.T., Begley, M.R., Levi, C.G., "Interaction of molten silicates with thermal barrier coatings under temperature gradients", Acta Materialia, 89 (2015) 396-407.

[13] Witz, G., Shklover, V., Steurer, W., Bachegowda, S., Bossmann, H.P., "High-temperature interaction of yttria stabilized zirconia coatings with CaO–MgO–$Al_2O_3$–$SiO_2$ (CMAS) deposits", Surface and Coatings Technology, 265 (2015) 244-249.

[14] Mechnich, P., W. Braue, and J. Smialek, “Solid-State CMAS Corrosion of an EB-PVD YSZ Coated Turbine Blade: $Zr^{4+}$ Partitioning and Phase Evolution”, Journal of the American Ceramic Society, 98(1) (2015) 296-302.

[15] Schfler, D.A, Choi, S.R., “CMAS Effects on Ship Gas-Turbine Components/Materials”, in Proceedings of ASME Turbo Expo 2018. 2018. Oslo, Norway.

[16] Smialek, J.L., Archer, F.A., Garlick, R.G. “The Chemistry of Saudi Arabian Sand: A Deposition Problem on Helicopter Turbine Airfoils, Advances in Synthesis and Processes”, 3rd Int. SAMPE Metals Conf. F.H. Froes, et al., Ed., October 20-22, 1992, p M63-M77

[17] Kim, J., Dunn, M.G., Baran, A.J., Wade, D.P., Tremba, E.L., “Deposition of Volcanic Materials in the Hot Sections of Two Gas Turbine Engines”, J. Eng. Gas Turbines Power,115 (3) (1993) 641-651.

[18] Toriz, F.C., Thakker A.B. Gupta, S.K., “Thermal Barrier Coatings for Jet Engines” J.ASME,88-GT-279(1988) (presented at the Gas Turbine and Aeroengine Congress Amsterdam, The Netherlands, June 6-9, 1988).

[19] Stott, F.H., de Wet, D.J., Taylor, R.,” The Effects of Molten Silicate Deposits on the Stability of Thermal Barrier Coatings for Turbine Applications at Very High Temperatures”, in F.H. Froes et al. (eds.) Advances in Synthesis and Processes, SAMPE, 3, 1992 M92-MI01

[20] Borom, M.P., Johnson, C.A., Peluso, L.A., “Role of environmental deposits and operating surface temperature in spallation of air plasma sprayed thermal barrier”, Surface and Coatings Technology, 86-87 (1996) 116-126

[21] Vidal-Setif, M.H., Chellah, N., Rio, C., Sanchez, C., Lavigne, O.,” Calcium-magnesium-alumino-silicate (CMAS) degradation of EB-PVD thermal barrier coatings:

Characterization of CMAS damage on ex-service high-pressure blade TBCs", Surface and Coatings Technology, 208 (2012) 39-45

[22] Lutz, B.S., Jackson, R.W., Abdul-Jabbar, N.M., Tolpygo, V.K., Levi, C.G. "Water Vapor Effects on the CMAS Degradation of Thermal Barrier Coatings", Oxidation of Metals, 88(1-2) (2017) 73-85.

[23] Naraparaju, R., Mechnich, P., Schulz, U., Mondragon Rodriguez, G.C., "The Accelerating Effect of $CaSO_4$ Within CMAS ($CaO$-$MgO$-$Al_2O_3$-$SiO_2$) and Its Effect on the Infiltration Behavior in EB-PVD 7YSZ", Journal of the American Ceramic Society, 99(4) (2016) 1398-1403.

[24] Fernandez, J., Gonzalez, F., Pesquera, C., Neves Junior, A., Mendes Viana, M., Dweck, J., "Qualitative and quantitative characterization of a coal power plant waste by TG/DSC/MS, XRF and XRD", J. Therm. Anal. Calorim. 125 (2016) 703-710

[25] Tolpygo, V., "Vapor-Phase CMAS-Induced Degradation of Adhesion of Thermal Barrier Coatings", Oxidation of Metals, 88(1-2) (2017) 87-96.

[26] Naraparaju, R., Hüttermann, M., Schulz, U., Mechnich, P. "Tailoring the EB-PVD columnar microstructure to mitigate the infiltration of CMAS in 7YSZ thermal barrier coatings", Journal of the European Ceramic Society, 37(1) (2017) 261-270.

[27] Rapp, R.A. "Hot corrosion of materials: a fluxing mechanism?", Corrosion Science 44 (2002) 209-221

[28] Rapp, R.A., Goto K.S., "The hot corrosion of metals by molten salts" In: R. Selman, J. Braunstein, editors. Second International Symposium on Molten Salts. Electrochemical Society; 1981, 159-177.

[29] Lux, H., “Saüren und Basen im schmelzfluss: die bestimmung der sauerstoffionen-konzentration“, Z. Elektrochem. 45(4) (1939) 303-309. (In German)]

[30] Jones, R.L., Williams, C.E. “Hot Corrosion Studies of Zirconia Ceramics”, Surface and Coatings Technology, 32 (1987) 349-358

[31] Duffy, J.A., Ingram, M.D., “Establishment of an Optical Scale for Lewis Basicity in Inorganic Oxyacids, Molten Salts, and Glasses”, J. Am. Chem. Soc., 93 (1971) 6448–6454.

[32] Chellah, N., Vidal-Setif, M.H., Petitjean, C., Panteix, P-J, Rapin, C., Vilasi, M., “Calcium-Magnesium-Alumino-Ssilicate (CMAS) Degradation of Thermal Barrier Coatings: Solubility of Different Oxides from $ZrO_2$-$Nd_2O_3$ System in a Model CMAS”, in Proc. HTCPM8, Les Embiez, France, (2012).

[33] Petitjean, C., Panteix, P.J., Rapin, C., Vilasi, M., Podor,R., “Electrochemical Behavior of Glass Melts: Application to Corrosion Processes”, Proc. Mater. Sci., 7 (2014) 101–110.

[34] Krause A.R., Garces, H.F., Senturk, B.S., Padture, N.P., “$2ZrO_2$-$Y_2O_3$ Thermal Barrier Coatings Resistant to Degradation by Molten CMAS. II. Interactions with Sand and Fly Ash”, J. Am. Ceram. Soc., 97 (2014) 3950–3957.

[35] Krause, A.R., Senturk, B.S., Garces H.F., Dwivedi G., Ortiz A.L., “$2ZrO_2$-$Y_2O_3$ Thermal Barrier Coatings Resistant to Degradation by Molten CMAS. I. Optical Basicity Considerations and Processing”, J. Am. Ceram. Soc. 97 (2014) 3943–3949.

[36] Lee, S.H., Min, D.J., “Influence of Basicity on Anodic Reaction in CaO-$SiO_2$-$Al_2O_3$ Melts” Journal of The Electrochemical Society, 164 (8) (2017) 5308-5314

[37] Moretti, R. “Polymerisation, basicity, oxidation state and their role in ionic modelling of silicate melts”, Annals of Geophysics 48 (4/5) (2005) 583-608

[38] Liu, J. Zhang, L., Liu, Q., Cheng, L., Wang, Y., "Calcium–magnesium–aluminosilicate corrosion behaviors of rare-earth disilicates at 1400 °C", Journal of the European Ceramic Society, 33 (15-16) (2013) 3419-3428

[39] Jiang, F., Cheng, L., Wang, Y. "Hot corrosion of $RE_2SiO_5$ with different cation substitution under calcium–magnesium–aluminosilicate attack" Ceramics International 43, 12 (2017) 9019-9023

Table 1: Chemical composition of CMAS1 and CMAS2

| | **Composition wt.% (mol.%)** | | | | | | | **Phases after cooling** | | |
|---|---|---|---|---|---|---|---|---|---|---|
| | **CaO** | **MgO** | **$Al_2O_3$** | **$SiO_2$** | **FeO** | **$TiO_2$** | **$CaSO_4$** | **Pyroxene** | **Anorthite** | **Melilite** |
| **CMAS1** | 22 (24.7) | 8 (12.3) | 18 (11.1) | 40 (41.6) | 10 (8.7) | 2 (1.6) | - | $[Ca,Mg,Fe,Al,Ti][Si,Al]_2O_6$ | $CaAl_2Si_2O_8$ | - |
| **CMAS2** | 17.6 (32.4) | 6.4 (11.2) | 14.4 (9.9) | 32 (37.3) | 8 (7.8) | 1.6 (1.4) | 20 | | - | $Ca_2(MgSi)_x(Al_2)_{1-x}[SiO_7]$ |

Table 2: Point analysis in wt.% of CMAS1 deposit after different exposures obtained from EPMA of figures 3 and 4

| Conditions | Figure | Position | Elements wt.% | | | | | | | |
|---|---|---|---|---|---|---|---|---|---|---|
| | | | Si | Fe | Ti | Mg | Ca | Y | Al | Zr |
| **Dry air** | **3a** | **1** | 20.9 | 17.4 | 2.7 | 11.0 | 33.5 | 0.4 | 13.5 | 0.6 |
| | | **2** | 39.5 | 4.7 | 0.4 | 2.9 | 22.4 | 0.6 | 29.0 | 0.0 |
| **Dry air + SO2** | **3b** | **3** | 0.8 | 58.3 | 1.3 | 19.3 | 1.4 | 0.2 | 18.6 | 0.2 |
| | | **4** | 22.3 | 17.1 | 2.5 | 11.5 | 33.8 | 0.4 | 12.1 | 0.4 |
| | | **5** | 40.8 | 5.1 | 0.8 | 1.9 | 22.9 | 0.0 | 27.9 | 0.0 |
| **Wet air** | **4a** | **6** | 23.9 | 17.8 | 2.7 | 10.6 | 32.2 | 0 | 12.6 | 0 |
| | | **7** | 24.6 | 16.6 | 2.1 | 10.1 | 32 | 0.3 | 13.6 | 0.6 |
| | | **8** | 28.4 | 5.2 | 0.2 | 0.9 | 29.1 | 0.1 | 35.8 | 0.1 |
| | | **9** | 29.4 | 3.9 | 0.3 | 0.6 | 29 | 0.5 | 35.6 | 0.6 |
| **Wet air + SO2** | **4b** | **10** | 25.8 | 16.6 | 2.1 | 10.7 | 31.5 | 0.5 | 12.2 | 0.6 |
| | | **11** | 24.8 | 17.4 | 2.3 | 10.4 | 31.4 | 0.4 | 12.5 | 0.8 |
| | | **12** | 30.5 | 4.2 | 0.3 | 0.7 | 28.7 | 0.1 | 35.5 | 0.1 |
| | | **13** | 30.3 | 3.6 | 0.1 | 0.5 | 28.9 | 0 | 36.4 | 0.1 |

**Table 3.** Summary of experimental observations to set out the discussion

| **Observation** | **CMAS1** | **CMAS2** |
|---|---|---|
| CMAS infiltration and wetting | Full infiltration under all atmospheres (figs. 5 and 7)<br><br>Wetting was considerably low and significant CMAS1 residue was found on top of the TBC under all conditions (fig. 1) | Fully infiltrated in all atmospheres. (figs. 1 and 8)<br><br>No residue of CMAS was found on top of TBC. This can be generally attributed to the lower viscosity of the melt in comparison to CMAS1 (fig 1). |
| $CaSO_4$ presence in YSZ | No presence/infiltration under any studied atmosphere (figs. 5 and 10) | Present only at the upper part of TBC along with other CMAS constituents.<br>Only detected in $SO_2$-containing atmospheres (both wet and dry) (fig. 9) |
| Reaction with exposure atmosphere | Less Si was present in the CMAS1 residue under wet conditions which can be associated with Si hydroxide evaporation (table 2) | Not possible to observe due to full infiltration of CMAS2 |
| Reaction with TBC | Higher Y depletion in the upper parts of TBC columns was observed under $SO_2$ containing atmospheres (fig 6) | Not possible to observe severe depletion in Y |
| Reaction with $Al_2O_3$ | Discontinuous spinel formation was observed at the YSZ/alumina interface under sulphur-containing atmospheres (fig 12.a) | A thicker and continuous spinel + anorthite layer has formed at the YSZ/alumina interface in all cases (fig 12.b) |

Figures

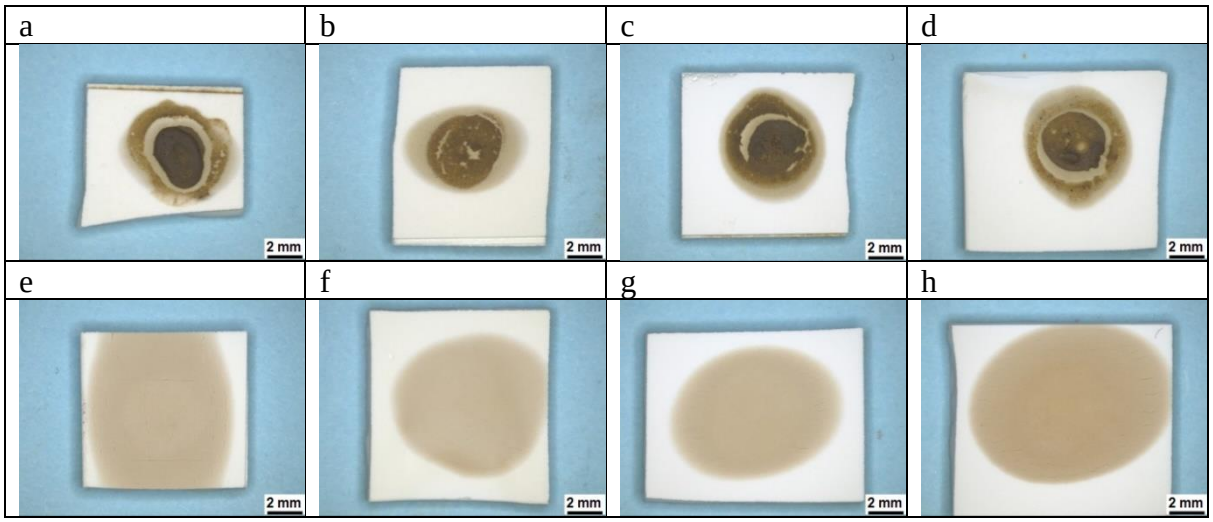


**Figure 1**. Stereo microscope macro figures of CMAS1-infiltrated YSZ after exposure at 1250°C for 5 hours in dry air (a), wet air (b), dry air with 0.5 vol. % $SO_2$ (c) and wet air with 0.5 vol. % $SO_2$ (d) and CMAS2-infiltrated YSZ in dry air (e), wet air (f), dry air with 0.5 vol. % $SO_2$ (g) and wet air with 0.5 vol. % $SO_2$ (h).

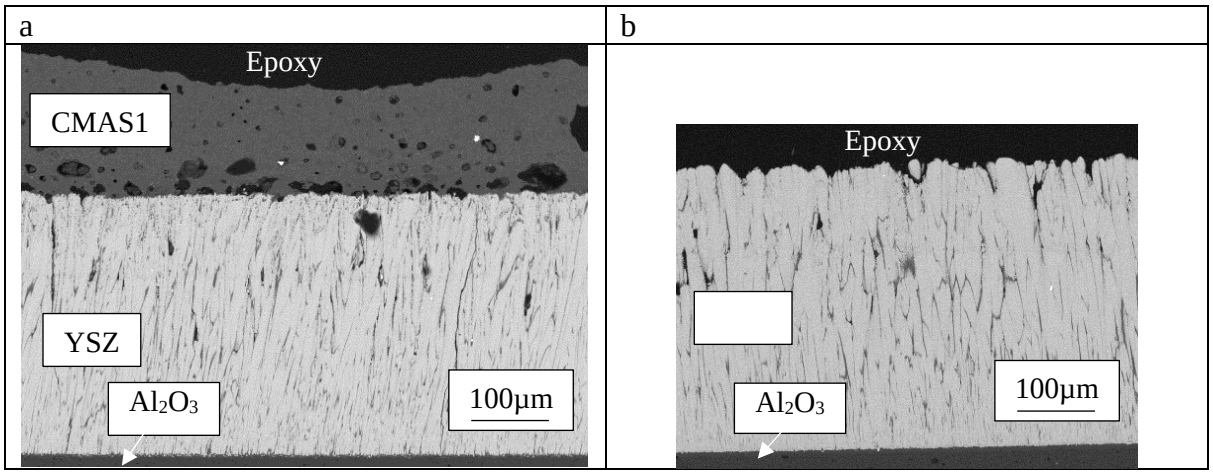


**Figure 2.** SEM cross section of YSZ coating infiltrated by CMAS1 showing residue deposit on top (a) and by CMAS2 (b) after exposure at 1250°C for 5 hours under synthetic air with 0.5 vol. % $SO_2$.

a

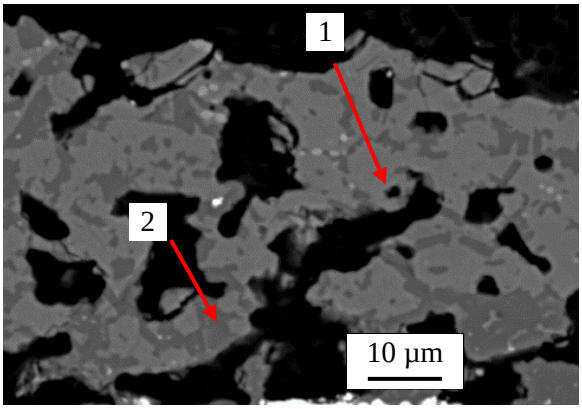
1
2
10 µm

b

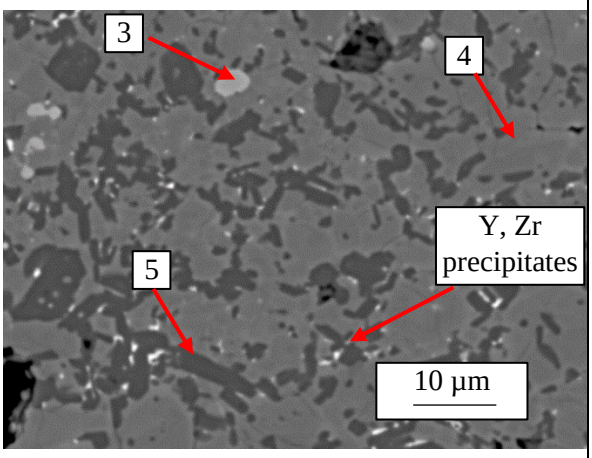
3
4
5
Y, Zr
precipitates
10 µm

c

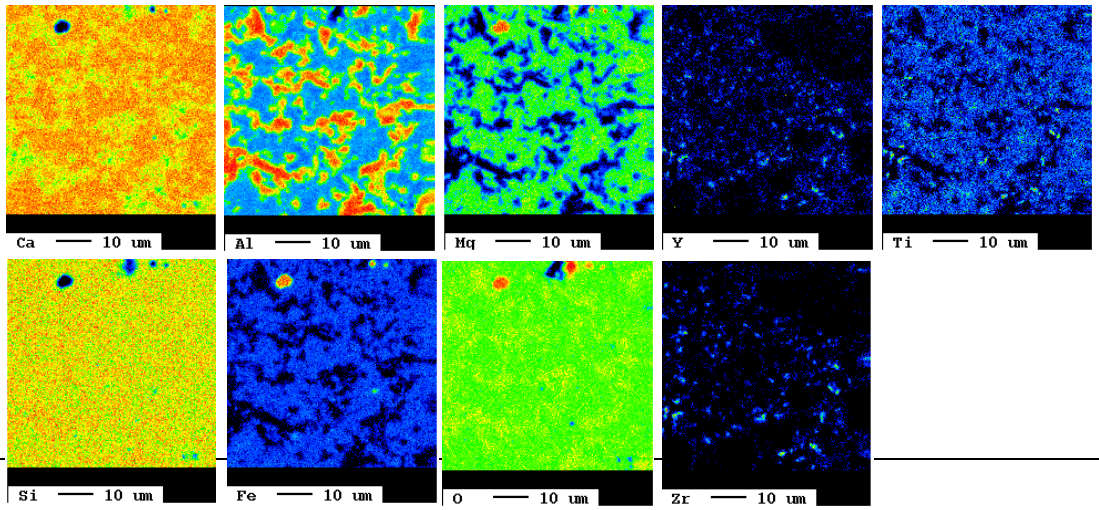
Ca 10 um
Al 10 um
Mg 10 um
Y 10 um
Ti 10 um
Si 10 um
Fe 10 um
O 10 um
Zr 10 um

**Figure 3.** BS-SEM cross-section of CMAS1 residue on top of infiltrated YSZ for 5h at 1250°C in dry synthetic air (a), and dry synthetic air with 0.5 vol.% of $SO_2$. (b), EPMA map of the latest (c), and point analysis of indicated spots obtained by EPMA analysis from a and b.

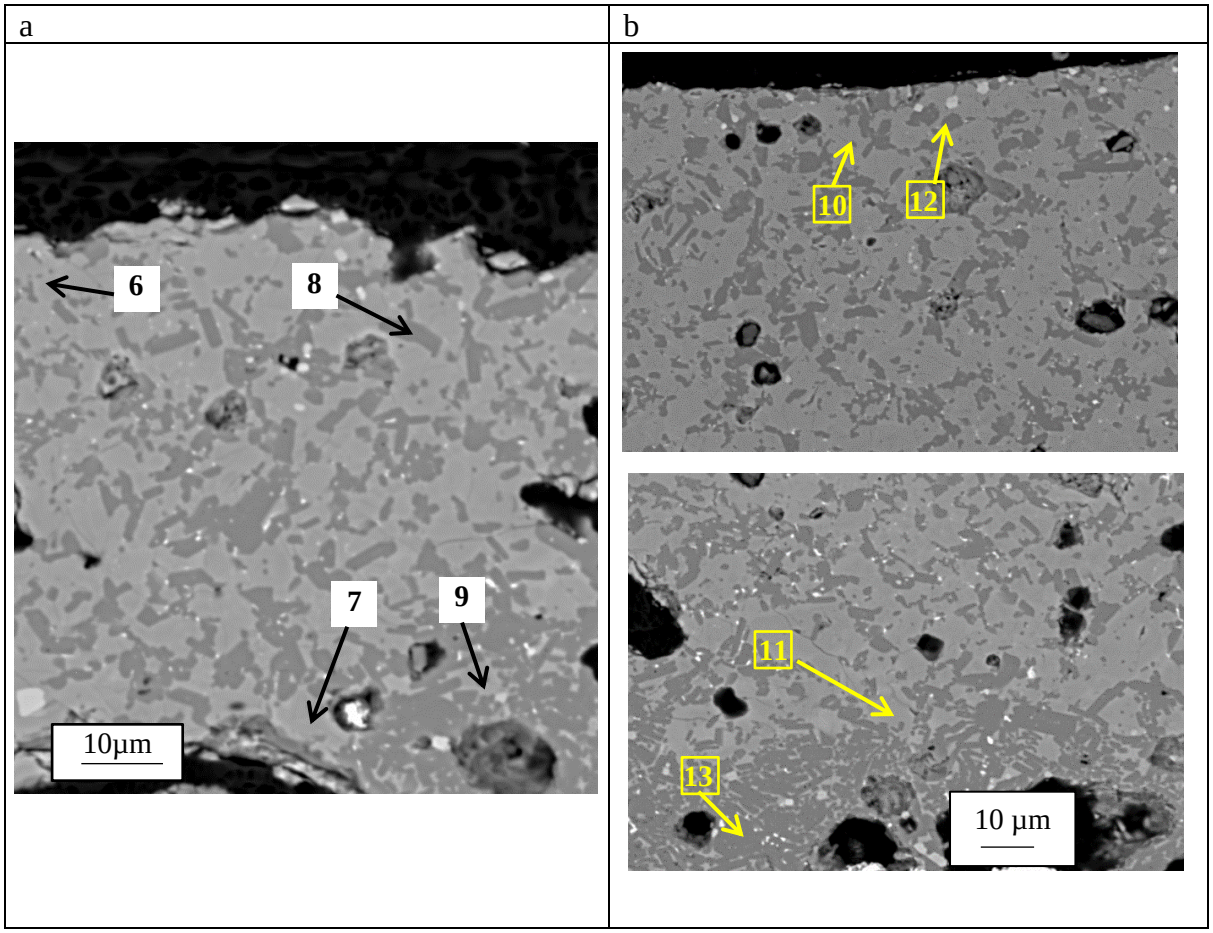

**Figure 4.** BS-SEM cross-section of CMAS1 residue on top of infiltrated YSZ after exposure of 5h at 1250°C in synthetic air with 10 vol.% of $H_2O$ (a) and synthetic air with 10 vol.% $H_2O$ and 0.5 vol.% $SO_2$. (b). Detail of CMAS1 residue/.

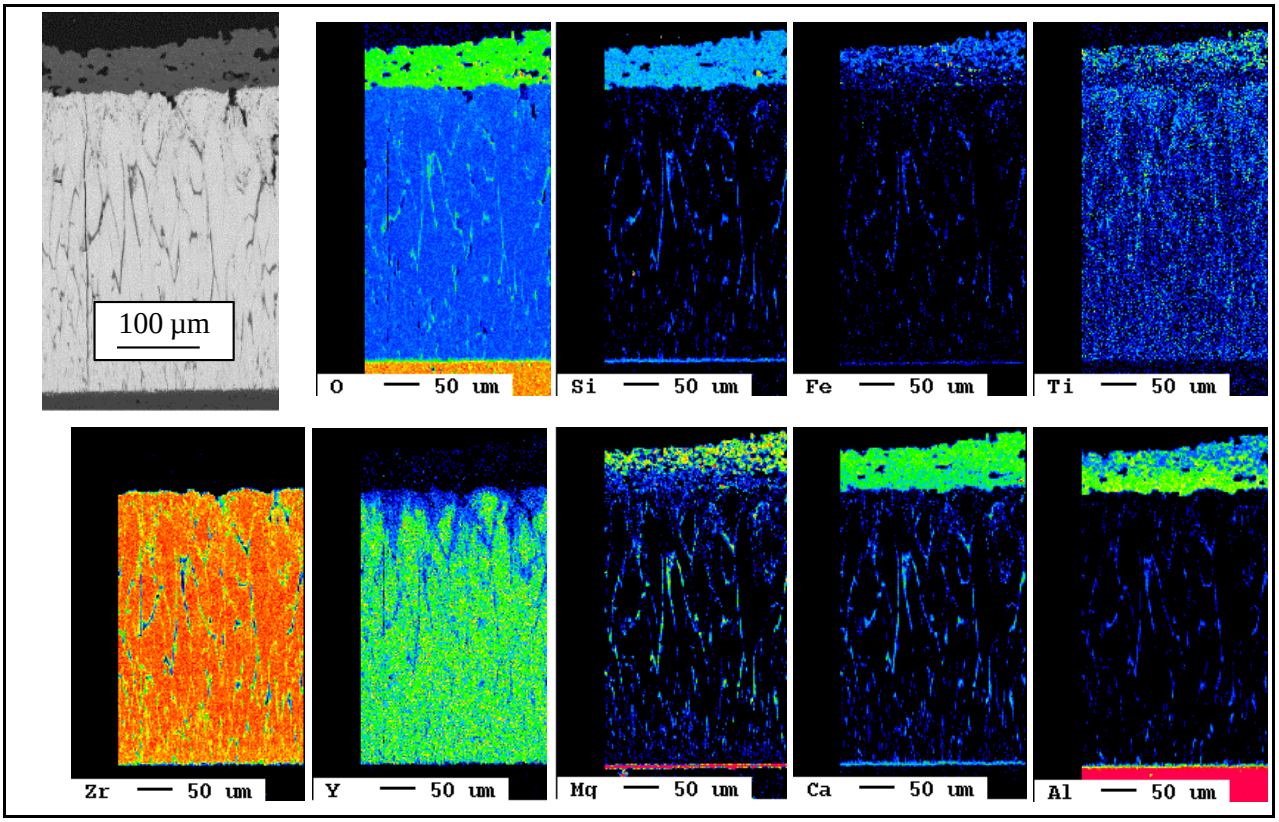


**Figure 5.** EPMA elemental distribution map of CMAS1-deposited YSZ after exposure of 5h at 1250°C in synthetic air with 10 vol.% $H_2O$.

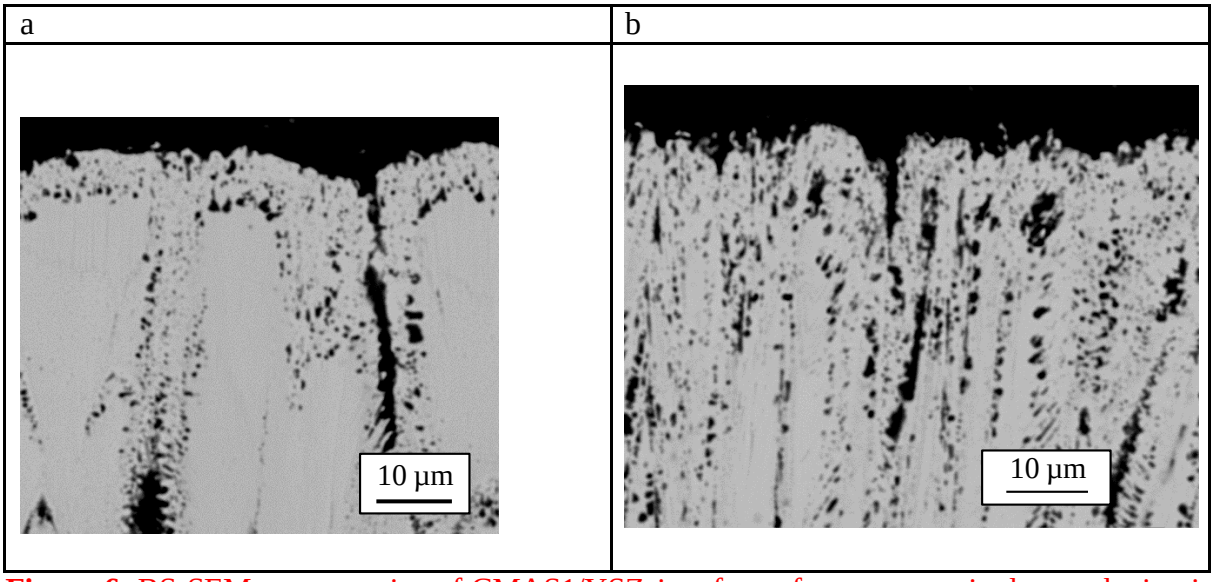


**Figure 6.** BS-SEM cross-section of CMAS1/YSZ interface after exposure in dry synthetic air (a), and dry synthetic air with 0.5 vol.% of $SO_2$ (b).

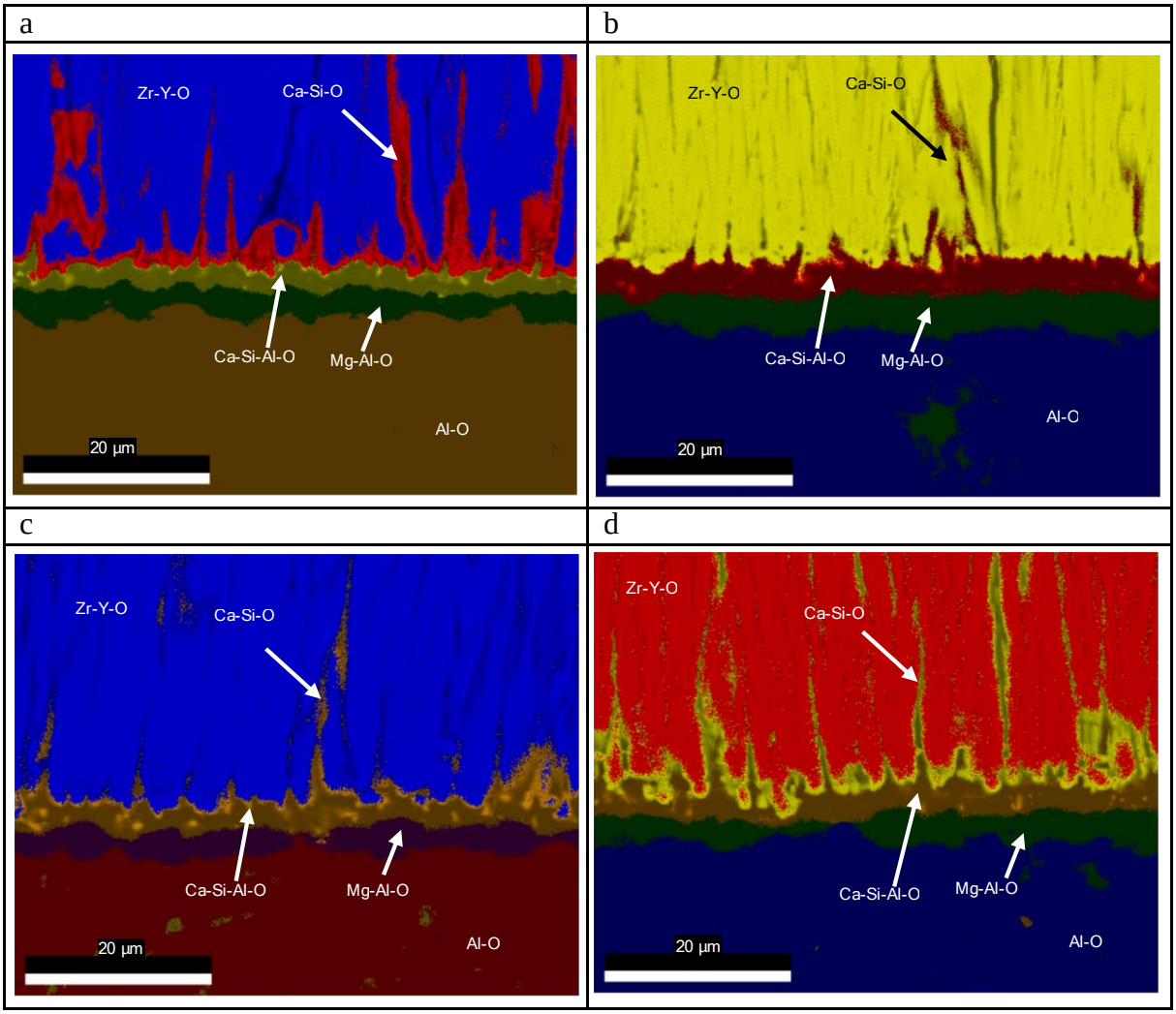


**Figure 7.** EDX elemental maps of the interface region between YSZ TBC and alumina substrate obtained from SEM cross-sections of CMAS1 after exposure of 5h at 1250°C in synthetic air (a), synthetic air with 10 vol.% of $H_2O$ (b), synthetic air and 0.5 vol.% $SO_2$ (c) and synthetic air with 10 vol.% of $H_2O$ and 0.5 vol.% $SO_2$ (d).

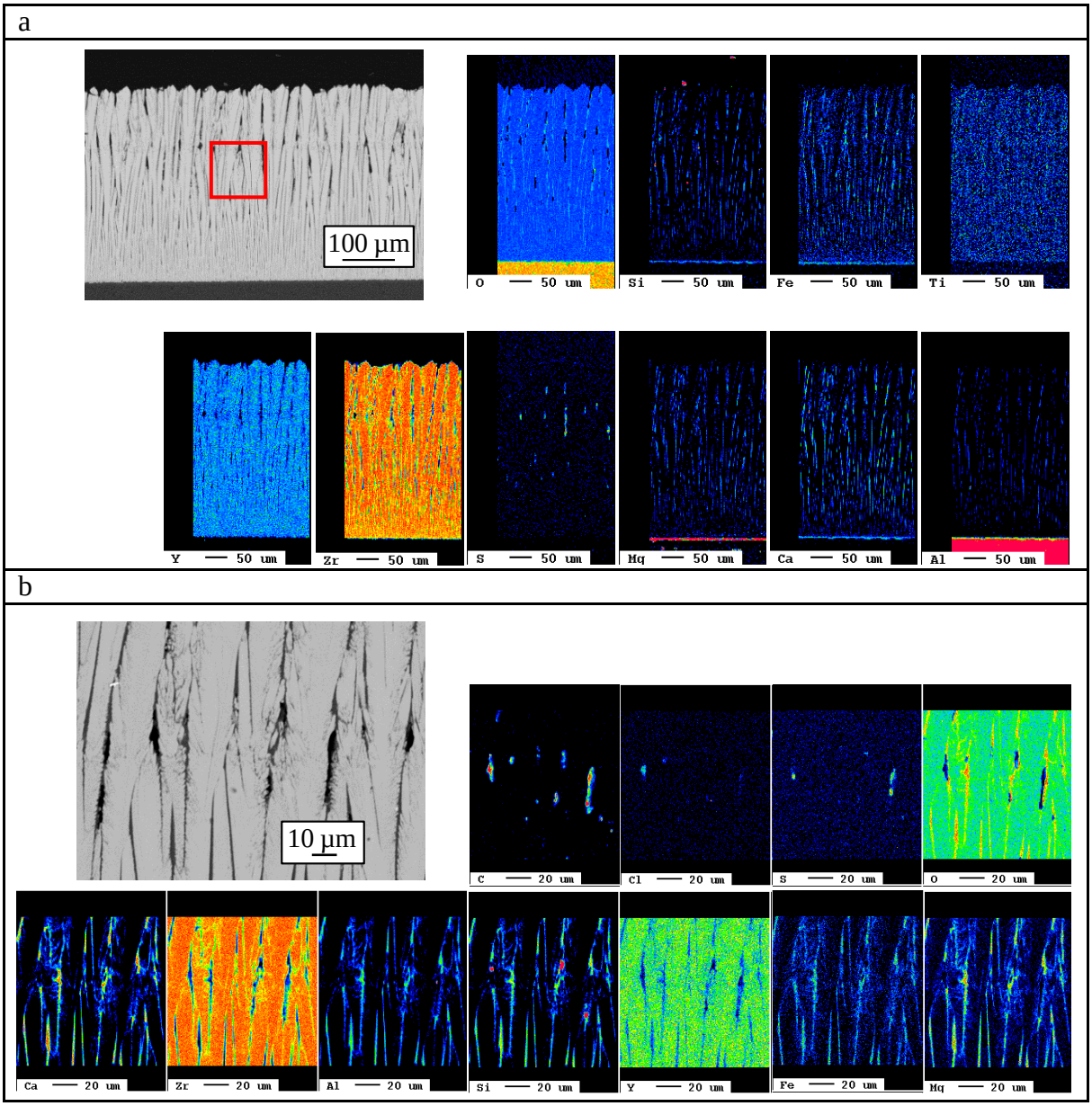


**Figure 8.** EPMA elemental distribution map of CMAS2-deposited YSZ after exposure of 5h at 1250°C in dry synthetic air. The square indicates the area in which EPMA point analysis was carried out (a), and detailed analysis of the indicated area (b)

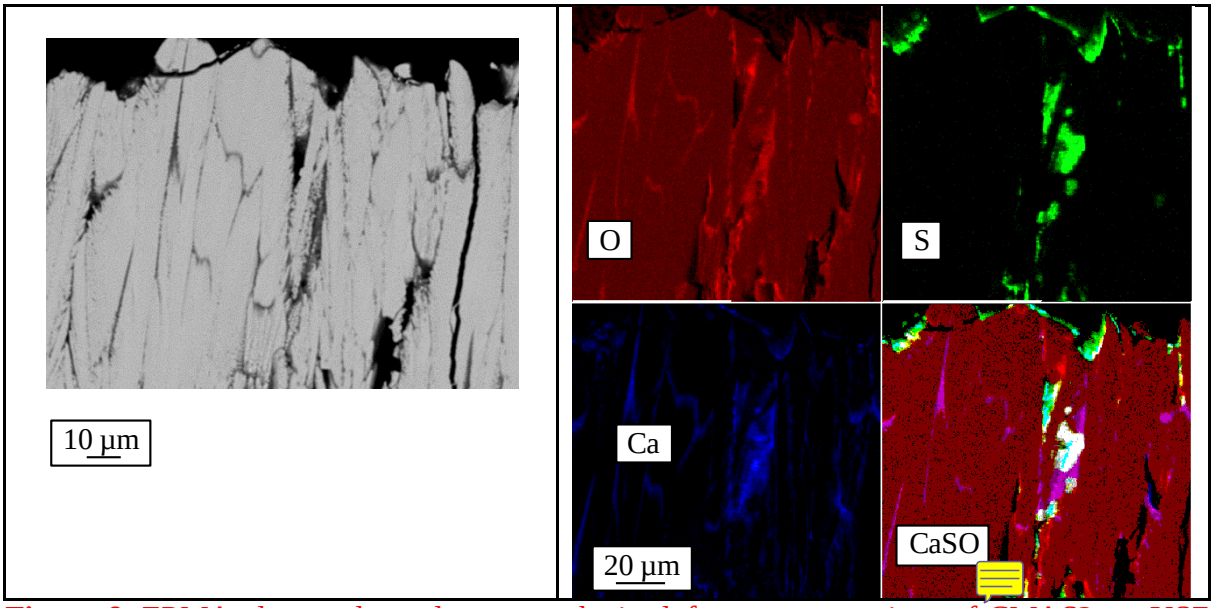


**Figure 9.** EPMA elemental overlay maps obtained from cross-sections of CMAS2 on YSZ after exposure of 5h at 1250°C in synthetic air with 10 vol.% of $H_2O$ and 0.5 vol.% $SO_2$. In this figure white colour indicates $CaSO_4$ presence.

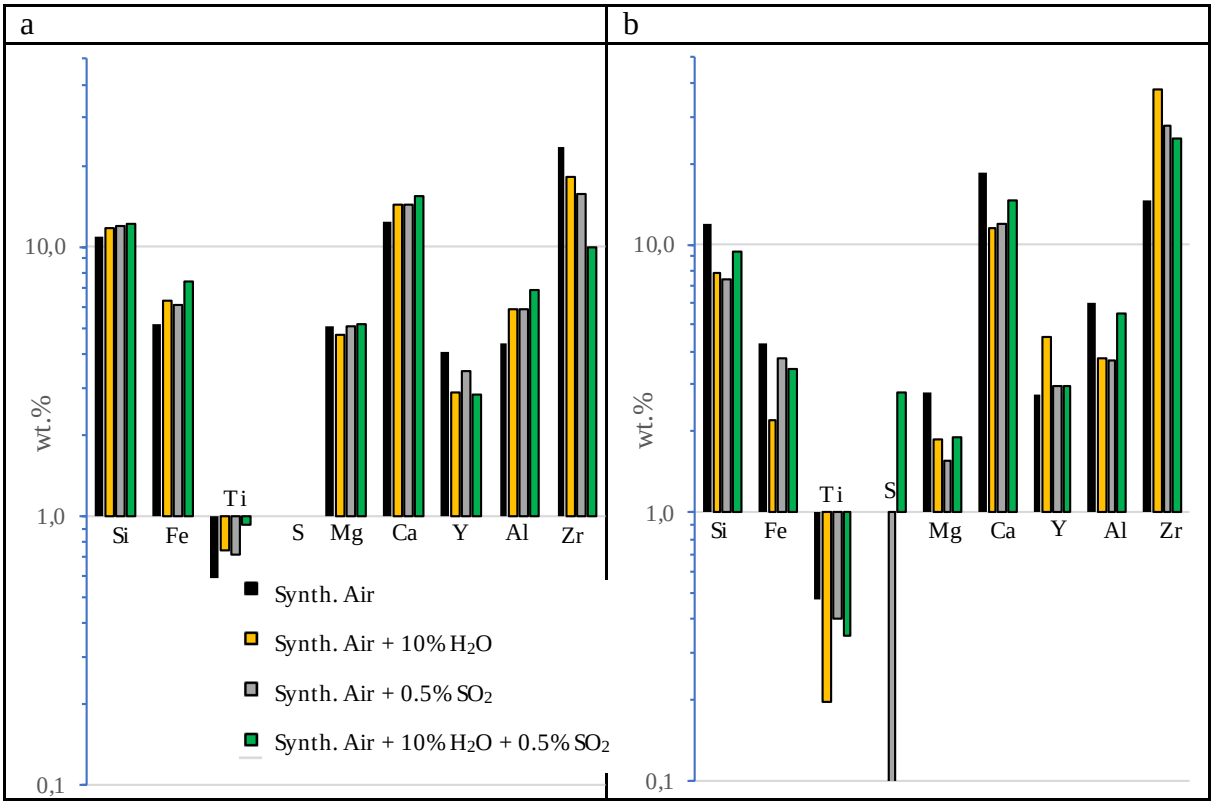


**Figure 10.** EPMA elemental analysis obtained from infiltrated CMAS rests in the middle of the YSZ for CMAS1 (a) and CMAS2 (b) in different atmospheres after 5h of exposure at 1250°C.

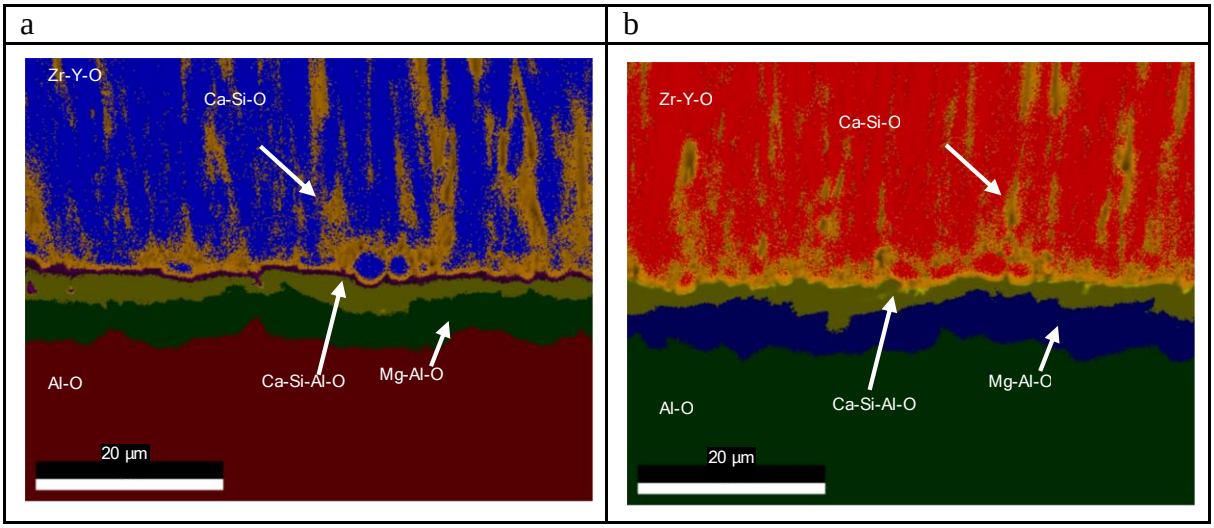


**Figure 11.** EDX elements combination map obtained from cross-sections of CMAS2-coated YSZ after exposure of 5h at 1250°C in synthetic air and 0.5 vol.% $SO_2$ (a) and synthetic air with 10 vol.% $H_2O$ and 0.5 vol.% $SO_2$ (b).

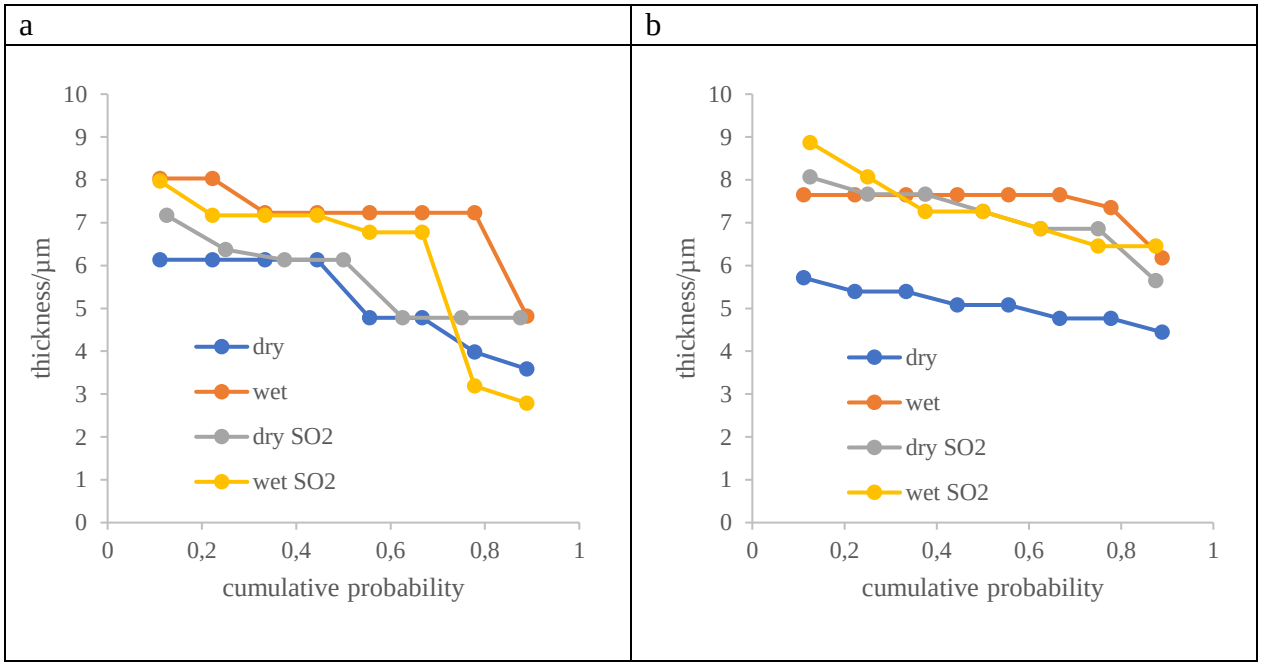


**Figure 12.** Cumulative probability plots of the spinel layer formed between YSZ and $Al_2O_3$ for the CMAS1 (a) and CMAS2 (b) cases.

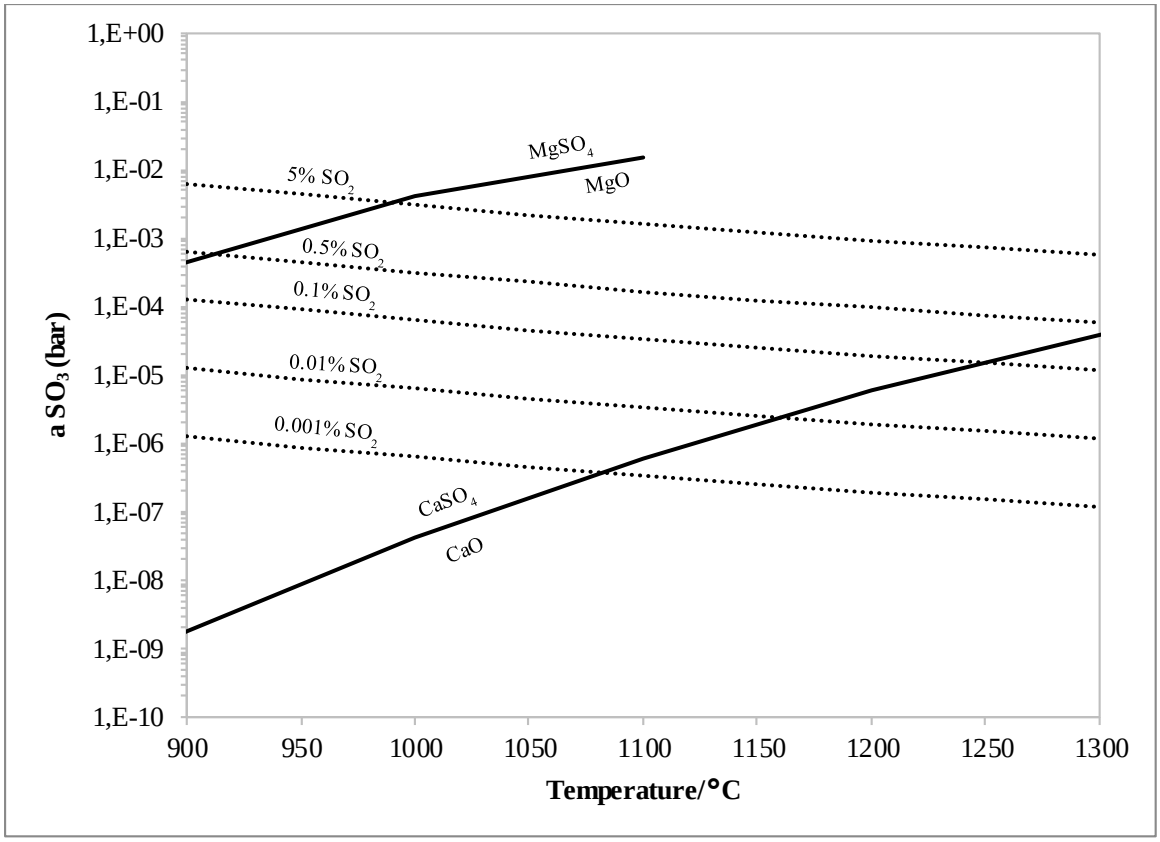


**Figure 13.** Ca and Mg sulphates stability between 900°C and 1300°C.

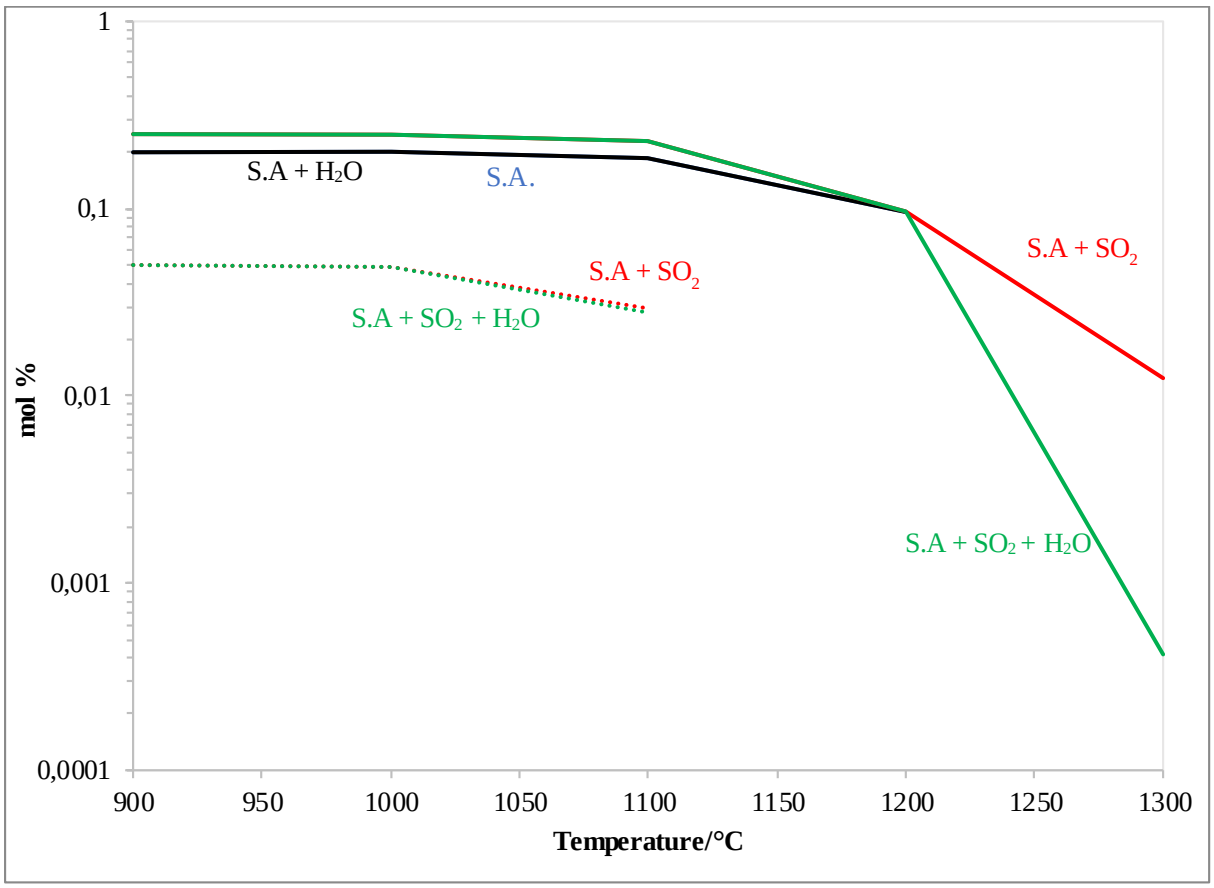


**Figure 14.** Calculated molar quantity of $CaSO_4$ in equilibrium for CMAS1 (dotted lines) and CMAS2 (solid lines) under the different tested atmospheres. S.A. is the abbreviation of synthetic air

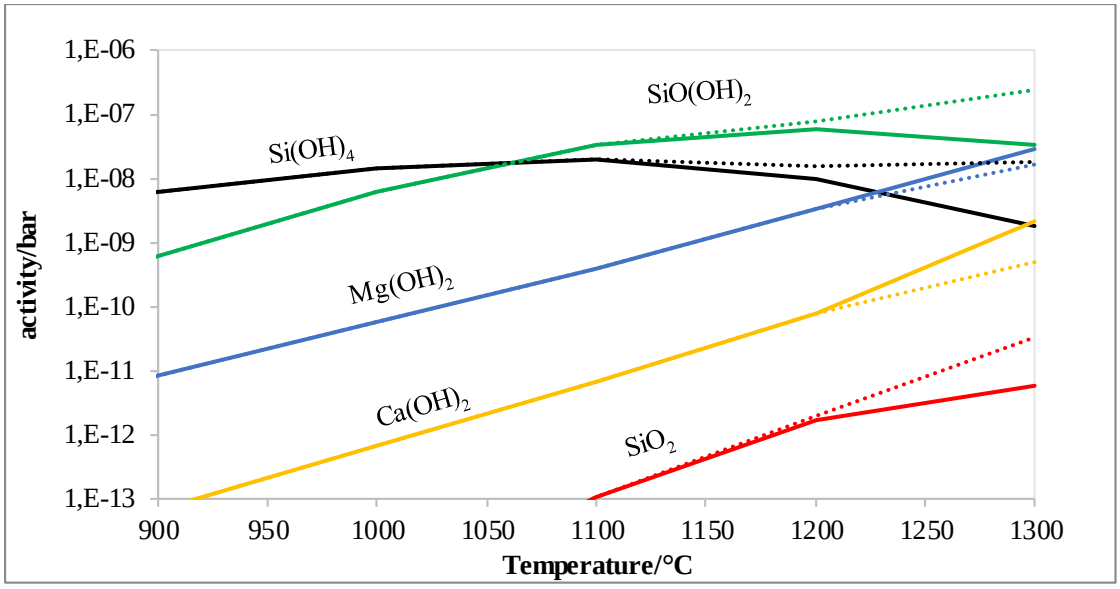


**Figure 15.** Gaseous species in 10 vol.% $H_2O$-containing synthetic air from CMAS1 (dotted line) and CMAS2 (continuous line).